


Article

Impact of Solidification on Inclusion Morphology in ESR and PESR Remelted Martensitic Stainless Steel Ingots

Ewa Sjöqvist Persson ^{1,*}, Sofia Brorson ², Alec Mitchell ³ and Pär G. Jönsson ⁴ ¹ Uddeholms AB, Uddeholm, SE-68385 Hagfors, Sweden² Swedish National Electrical Safety Board, Box 4, 68121 Kristinehamn, Sweden; Sofia.Brorson@Elsakerhetsverket.se³ Department of Materials Engineering, University of British Columbia, Vancouver, BC V6T 1Z4, Canada; alecm@mail.ubc.ca⁴ Materials Science and Engineering, KTH, Royal Institute of Technology, SE-10044 Stockholm, Sweden; parj@kth.se

* Correspondence: ewa.persson@uddeholm.com

Abstract: This study focuses on the impact of solidification on the inclusion morphologies in different sizes of production-scale electro-slag remelting (ESR) and electro-slag remelting under a protected pressure-controlled atmosphere, (PESR), ingots, in a common martensitic stainless steel grade. The investigation has been carried out to increase the knowledge of the solidification and change in inclusion morphologies during ESR and PESR remelting. In order to optimize process routes for different steel grades, it is important to define the advantages of different processes. A comparison is made between an electrode, ESR, and PESR ingots with different production-scale ingot sizes, from 400 mm square to 1050 mm in diameter. The electrode and two of the smallest ingots are from the same electrode charge. The samples are taken from both the electrode, ingots, and rolled/forged material. The solidification structure, dendrite arm spacing, chemical analyzes, and inclusion number on ingots and/or forged/rolled material are studied. The results show that the larger the ingot and the further towards the center of the ingot, the larger inclusions are found. As long as an ingot solidifies with a columnar dendritic structure (DS), the increase in inclusion number and size with ingot diameter is approximately linear. However, at the ingot size (1050 mm in diameter in this study) when the center of the ingot converts to solidification in the equiaxial mode (EQ), the increase in number and size of the inclusions is much higher. The transition between a dendritic and an equiaxial solidification in the center of the ingots in this steel grade takes place in the region between the ingot diameters of 800 and 1050 mm.



Citation: Persson, E.S.; Brorson, S.; Mitchell, A.; Jönsson, P.G. Impact of Solidification on Inclusion Morphology in ESR and PESR Remelted Martensitic Stainless Steel Ingots. *Metals* **2021**, *11*, 408. <https://doi.org/10.3390/met11030408>

Academic Editor: Mark Schlesinger

Received: 29 January 2021

Accepted: 21 February 2021

Published: 2 March 2021

Keywords: ESR; PESR; inclusions; solidification; SEM; stainless steel

Publisher's Note: MDPI stays neutral with regard to jurisdictional claims in published maps and institutional affiliations.



Copyright: © 2021 by the authors. Licensee MDPI, Basel, Switzerland. This article is an open access article distributed under the terms and conditions of the Creative Commons Attribution (CC BY) license (<https://creativecommons.org/licenses/by/4.0/>).

1. Introduction

Uddeholms AB specializes in producing tool steels. The steels are manufactured in the Hagfors steel mill. The production is approximately 100,000 tons per year in the steel melting shop. The steel grades are mainly hot work steels, cold work steels, and plastic mould steels. About 55% of the steel grades are electro-slag remelted (ESR) or electro-slag remelted under a protected pressure-controlled atmosphere (PESR). The reason to choose ESR or PESR remelting processes could either be to reach higher mechanical properties (more homogenous material) or a better polishability of the steel.

In order to optimize the properties, (who are directly related to the microstructure), of a given steel grade, it is important to understand the evolution of the microstructure during the solidification and subsequent cooling to room temperature [1]. The main variables controlling the microstructure evolution include the interface velocity, thermal gradient, alloy composition, and nucleation potential [1]. These variables will change considerably

during the columnar/equiaxial transition (CET). Therefore, it is important to know during which circumstances during remelting of an ingot, this transition will take place.

In this investigation, studies on the solidification structure, dendrite arm spacing, and inclusion number per area are made on an electrode (300 mm square) and ESR and PESR ingots (400 mm square—1050 mm in diameter) are performed. The steel grade is a commonly used martensitic stainless steel.

Previous studies on non-metallic inclusions (NMI) and cleanliness in ESR or PESR remelted ingots are presented in Table 1 [2–27]. It can be seen that the majority of studies by other authors are executed in laboratory or pilot scales (from 0.8 up to 50 kg experimental trials) with focus on steel grades other than martensitic stainless tool steels. The inclusions found in laboratory-scale trials are usually in the size range of 1–5 μm , but more often $\leq 2 \mu\text{m}$. However, in industrial-size ingots, significantly larger inclusions can be found, especially if larger sample areas are analyzed. Therefore, for reliable evaluations of the characteristics of NMI (especially larger size inclusions) in production-scale trials, only investigations of NMI in laboratory and pilot experiments are not sufficient. In this study of inclusions in production-scale ingots, the analyzed area is about 6000–6500 mm^2 per sampling position (about 2000 mm^2 for the ingots). On the forged or rolled areas, approximately 1–3 inclusions between 20 and 30 μm per sample are detected. The sample areas in laboratory-scale trials are usually about 100 mm^2 . According to Franceschini et al. [28], an analyzed surface of 5000 mm^2 is suitable for evaluating the cleanliness for remelting processed samples, to compare with air samples where 1000 mm^2 is sufficient.

Table 1. Previous studies on inclusions in electro-slag remelting (ESR) or electro-slag remelting under protective pressure-controlled atmosphere (PESR) remelted.

Year	Author	Steel	Scale	Diameter/Width	Inclusions Size	Ref.
1971	D.A.R. Kay et al.	N.A.	N.A.	N.A.	N.A.	[1]
1980	Z.B. Li et al.	N.A.	N.A.	N.A.	N.A.	[2]
2012	C.-B. SHI et al.	NAK80 die steel	N.A.	N.A.	N.A.	[3]
2012	C.-B. SHI et al.	Die steel	Laboratory	N.A.	N.A.	[4]
2012	C.-B. SHI et al.	High-al steel	N.A.	N.A.	<5 μm	[5]
2012	X.C. Chen et al.	Inconel 718	N.A.	N.A.	CN 5–15 μm	[6]
1969	B.C. Burel	steel, iron	Laboratory	Mould 77 mm	<15 μm	[7]
1974	A. Mitchell et al.	oxygen containing iron, iron-OFHC copper	Laboratory	Mould 76.2 mm	1–5 μm	[8]
1976	J.C.F. Chan et al.	Stainless steel	Laboratory	Electrode 35 mm	N.A.	[9]
2013	C.-B. SHI et al.	Die steel, superalloys	Laboratory	N.A.	N.A.	[10]
2013	Y. Dong et al.	Cold rolls steel MC5	Laboratory 800 g	N.A.	N.A.	[11]
2014	Y.-W. Dong et al.	Die steel CR-5A	Laboratory 800 g	N.A.	N.A.	[12]
2013	C.-B. SHI et al.	H13 die steel	Laboratory, 50 kg	Electrode 90 mm	abt 2 μm	[13]
2015	R. Scheinder et al.	Hot work steel abt H11	Pilot	Electrode 101.5 mm	N.A.	[14]
2016	C.-B. SHI et al.	High-Carbon 17% Cr Tool Steel	Pilot	PESR mould 170 mm	abt 5 μm	[15]
2017	G. Du et al.	H13 die steel	Pilot	ESR mould 300 mm	0–15 μm , >15 μm	[16]
2014	L.Z. Cang et al.	N.A.	Pilot 15 kg	Mould abt 105 mm		[17]
2019	C.-B SHI et al.	Si-Mn killed steel \approx H13	Pilot	PESR 95 mm	1–3 μm , few > 3 μm	[18]
2013	G. Reiter et al.	abt H11, H13 die steel, martensitic Cr-Ni steel	Industrial	N.A.	ASTM E45 Heavy	[19]

Table 1. Cont.

Year	Author	Steel	Scale	Diameter/Width	Inclusions Size	Ref.
2014	E.S. Persson et al.	Martensitic stainless steel	Industrial	Moulds 400–1050 mm	8–30 μm	[20]
2016	E.S. Persson et al.	Martensitic stainless steel	Industrial	Moulds 400–1050 mm	N.A.	[21]
2017	H. Wang et al.	H13 die steel	Laboratory	Electrode 25 mm	abt 1–2 μm	[22]
2017	E.S. Persson et al.	Martensitic stainless steel	Industrial	Moulds 400–500 mm	8–45 μm	[23]
2017	E.S. Persson et al.	Martensitic stainless steel	Industrial	ESR mould 300 mm	8–20 μm	[24]
2018	E.S. Persson et al.	Martensitic stainless steel	Industrial	ESR mould 300 mm	8–20 μm	[25]
2020	E.S. Persson et al.	Martensitic stainless steel	Industrial	ESR mould ca 500 mm	8–22.4 μm	[26]

The earlier and most generally accepted theories assumes that the inclusions in the electrode will be rejected to the surface of the electrode tip to be incorporated into the liquid process slag [9,21–25,29]. The steel melt will then seek equilibrium with the process slag, so that new, different oxygen levels in the liquid steel pool will be obtained. During solidification, new inclusions are re-precipitated as secondary inclusions in the ESR or PESR ingot.

Recently, Sjöqvist Persson et al. [26,27] stated that the inclusions in a remelted ingot can be primary, semi-secondary, or secondary inclusions. The primary inclusions are suggested to have been trapped in a fallen steel drop. Furthermore, the semi-secondary have a core of an un-melted Mg-spinel (Al–Mg oxide) that has survived from the electrode together with an outer layer with a composition corresponding to the ESR process slag [25–27]. Specifically, this could, e.g., be MgAl_2O_4 inclusions (with a low content of MgO) and Al_2O_3 inclusions formed in the liquid metal pool as a result of the reactions between alloying elements and dissolved oxygen.

The critical point for growing and clustering of the newly nucleated/formed secondary inclusion, as well as the growth and clustering of the primary and the semi-secondary inclusions, is the local solidification time (LST) [30,31]. This, in turn, depends on the melting rate, immersion depth of the electrode tip in the slag bath, the electrode/ingot ratio, and time for heat transfer from the center to the surface of the ingot. In reality, it means that the larger the ESR ingot size the longer the LST. At a critical LST value, the solidification will turn from a columnar dendritic (CD) to an equiaxial structure (EQ), which is called the columnar/equiaxial transition (CET). The parameters, which cause the transition, are the alloy segregation characteristics, freezing rate, undercooling, and the presence or absence of nucleating sites for the equiaxial crystals [32]. If the ingot structure changes from CD to EQ, the consequent competing growth and possible movement of the EQ crystals leads to a random formation of pockets of segregated inter-dendritic liquid. As a result, the homogenization temperature normally used for the steel grade may lie above the critical temperature where the process starts to produce porosities due to the lower melting point in the last solidified material. The result is that the ingot cannot be successfully homogenized [32]. Due to the same reason, the segregated liquid also leads to microstructure effects in many alloys that produce primary precipitates (NMI and inter-metallic inclusions (IMI)), which are not changed by subsequent mechanical or thermal processing [32]. At this point (CET), the steel will be more segregated and the inclusions will have sufficient time to grow and agglomerate.

A calculation shows that an alloy with a LST value >3500 s is likely to solidify in the equiaxial mode [33]. In Figure 1, results from laboratory trials by Mitchell are displayed [33]. They indicate that the critical point could be reached at an ingot size of 1050 mm in diameter.

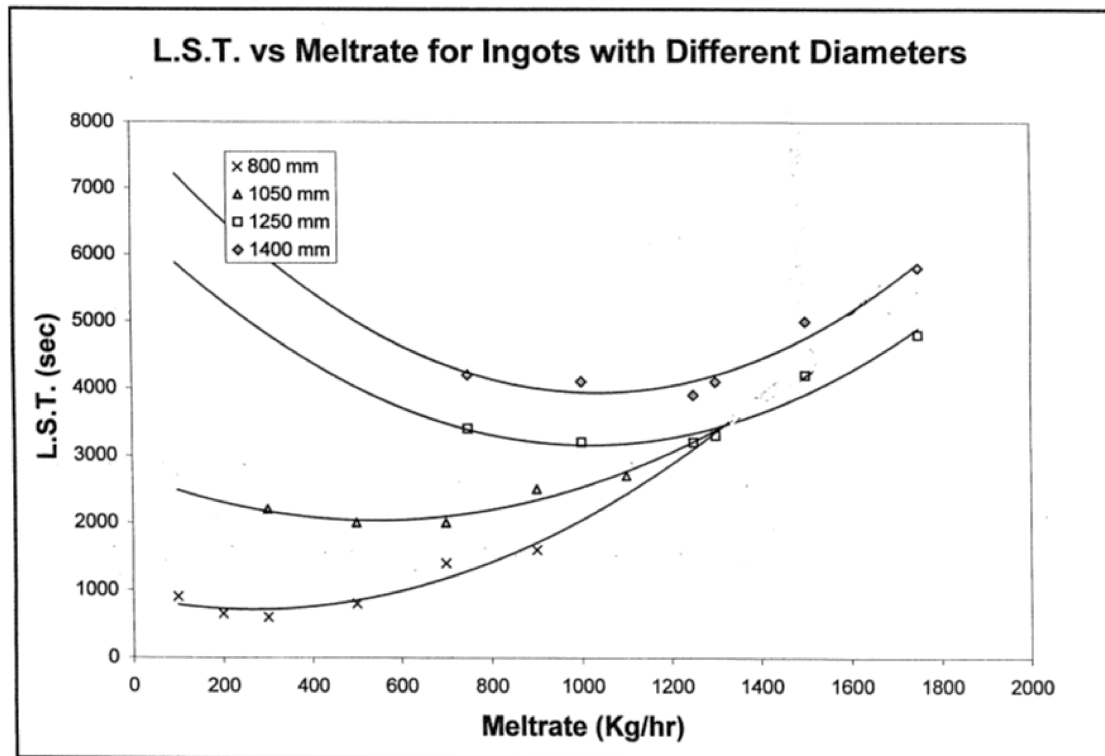


Figure 1. Longest Solidification Time (LST) versus melt rate for ingots with different diameters [33].

As long as the ingot solidifies in a columnar-dendritic manner, the angle between the columnar dendrites direction and the bottom of the liquid steel pool is 90° at the center position of the ingot [30,31,34].

An investigation of the solidification of a 750 mm in diameter ESR/PESR remelted ingot at different melt rates was made at Breitenfeldt Edelstahl AG in Austria [35]. The results showed that the higher the melt rate, the deeper liquid the steel pool. However, even at the highest used melt rate (standard melt rate +100 kg/h), the solidification was columnar-dendritic from the surface to center. At the same time, the number and size of the inclusion increased with a higher melt rate/deeper pool.

Borodin et al. [36] investigated the solidification of 400 mm in diameter ESR ingots remelted using different melt rates and on a 550 mm in diameter ingot remelted using one melt rate. They found disoriented dendrites (equiaxial solidification) in the 400 mm in diameter ingot, but not in the 500 mm in diameter ingot. However, the used melt rates were much higher (510 and 670 kg/h for the 400 mm in diameter ingot and 700 kg/h for the 500 mm in diameter ingot), than the “rule of thumb” of an estimated melt rate (kg/h) of $\pm 80\%$ of the ingot diameter (mm). The electrodes used were described to have a very convex shape (probably mostly due to the high melt rate and also depending on the use of a low electrode/ingot ratio), which not is the case in present high-quality ESR remelting processes.

According to Xuan et al. [37], the most important factors for an inclusion to be captured in a process slag are its size and flotation speed in the steel. According to this proposal, in the case of a vacuum-treated steel shop charge, with different slag compositions and movements of the steel, inclusions larger than approximately $20\ \mu\text{m}$ in diameter should be captured in the process slag. The critical size for flotation of an inclusion from the molten steel pool in the ESR/PESR processes to the process slag, along with the chemical

composition of the slag and the size of the inclusion will also depend on the movements in the liquid steel pool. The movements in the liquid steel pool depend on the size of the ingot and the depth of the steel pool. The depth of the steel pool is dependent of the melt rate (kg/h), the immersion depth of the electrode in the slag, and the electrode/ingot diameter relation. The terminal velocity of a Mg spinel inclusion 50 μm in diameter rising in a liquid steel is approximately 5×10^{-4} m/s given the computed ingot pool pattern [38]. This implies that any inclusion removal is determined by a balance between the probabilities of being exposed to the slag/ingot interface or being trapped in the solidifying metal as dictated by the bulk metal flow of the liquid ingot pool. Inclusions (depending on their size and density) will be trapped in the flow pattern, many never reaching the steel/slag interface. According to this model, the contribution of inclusion refining through flotation is much smaller than what has previously been estimated. Further studies are needed to better understand this mechanism during ESR/PESR processes. However, it can be postulated, due to the shorter LST, i.e., shorter time for the steel pool to be liquid, that the smaller the ingot size, the less the overall possibility for flotation of inclusions. In contrast, a previous study [21,22] showed that the larger the ESR or PESR ingot, the more and larger inclusions could be found.

According to Fredriksson et al. [34], the surface of an as cast ingot solidifies in a different manner as compared to an ESR or PESR ingot. In an as-cast ingot, the melt close to the mould cools down rapidly to a temperature beneath the critical temperature for nucleation of crystals. This results in many nuclei, which form a surface zone consisting of equiaxial crystals. The dendrites grow $<90^\circ$ up against the top center of the ingot, controlled by the temperature gradient. In ESR and PESR remelted ingots, the surface zone of equiaxial crystals does not usually exist. Instead, the surface zone consists of long radially oriented crystals. The long radial format of the dendrites is due to that the dendrites grow with the solidification front along the surface. Therefore, it can be stated that in ESR and PESR processes, no strongly undercooled surface zones exist that result in the formation of equiaxial crystals. During solidification, however, due to the cooling effect from the mould, there is a finer dendrite structure in the surface than in the center of the ingot. The long crystals along the surface give the ESR and PESR ingots a smooth and good surface.

Electrode inclusions are modified by several mechanisms, i.e., dissolution in the steel as the electrode melts, dissolution in the slag at the electrode/slag interface, dissolution in the slag during the droplet fall, and flotation in the ingot pool followed by dissolution in the slag at the ingot/slag interface. This study does not define the role of each of these individual processes but presents the overall result of them as it pertains to the final inclusion content.

The current study focuses on the solidification process and the oxide inclusions in a production-scale electrode, relative to ESR and PESR ingots of different sizes in a stainless martensitic steel. The aim is to relate the solidification and ingot size to the number and type of inclusions found. In order to optimize process routes for different steel grades, it is important to define the inclusion characteristics in ESR and PESR materials.

2. Materials and Methods

The material studied was from one ingot-cast consumable electrode $300 \times 300 \text{ mm}^2$ (denoted as the CE-300 sample), one ESR remelted ingot $400 \times 400 \text{ mm}^2$ (denoted as the ESR-400 sample), and three PESR remelted ingots 500, 800, and 1500 mm in diameter (denoted below as the PESR-500, -800, and -1050 samples, respectively). The electrode, the ESR-400, and the PESR-500 were cast from the same initial steel charge. The difference between the ESR and PESR process is that the ESR here represents a multiple-electrode remelting process (involving electrode changes), which is performed in a moving mould, in an open furnace under an air atmosphere, using a continuous aluminum deoxidation. In contrast, the PESR process is a single-electrode remelting process using a static mould and an inert pressure-controlled atmosphere.

A typical composition of martensitic stainless steel used in this study is as follows: C 0.38%, Si 0.9%, Mn 0.45%, Cr 13.6%, and V 0.28%. In the ESR and PESR trials, a common process slag was used containing about one-third each of CaO, CaF₂, and Al₂O₃, and including $\approx 3\%$ MgO and $\approx 1\%$ SiO₂.

The steel samples were taken from horizontal slice/slices of the electrode and ingots as follows: top (T), middle (M), and bottom (B) for the electrode, two samples taken at positions in between top and bottom (1,2) for the ESR-400, and one middle sample (M) for the PESR ingots, respectively, see Figure 2a,b. The cross-sections have been cut in order to study the solidification structures and dendrite arm spacings. The samples from the electrode and ingots cover the full distance/radius from the corner/surface to the center. A schematic presentation of the positions of the macro samples for both the square electrode, ESR ingot, and PESR ingots can be seen in Figure 2d,e. Each sample with a dimension of $\approx 150 \times 100 \times 15 \text{ mm}^3$ was ground and polished using a $3 \mu\text{m}$ diamond finish and etched in a solution consisting of either 50% HCl in water at 50°C or using Björk's etchant followed by rinsing in ammonia. Thereafter, the secondary arm spacing (SDAS), at different positions on the cross-sections was measured, as described below.

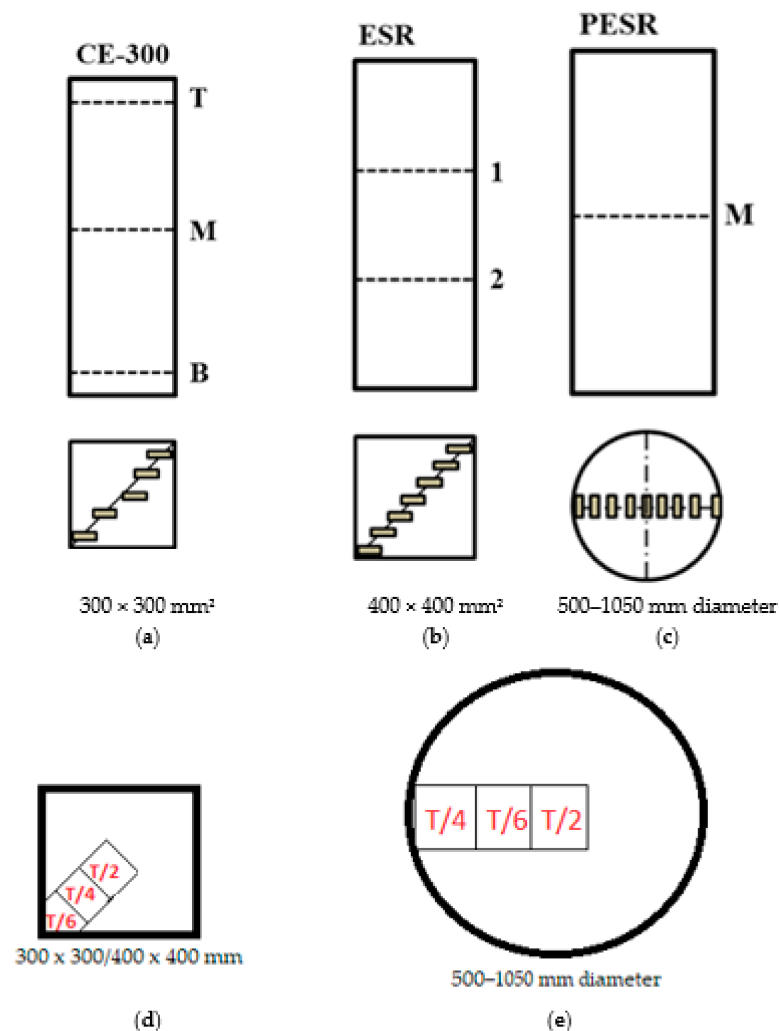


Figure 2. Schematic illustration of horizontal slices and position of the micro sample on (a) the consumable electrode, CE-300, (b) ESR remelted ingots, and (c) PESR remelted ingots. Schematic illustration of the positions of the macro samples for (d) the electrode $300 \times 300 \text{ mm}^2$, for the electroslag remelted (ESR) ingot $400 \times 400 \text{ mm}^2$, and (e) the pressure electroslag remelted (PESR) ingots 500–1050 mm in diameter. Position T/2 is located in the center of the electrode/ingot, T/4 in between the center and the surface/corner, and T/6 in between position T4 and the surface/corner.

Longitudinal sections were cut out from the cross-sections from the 500, 800, and 1050 mm in diameter PESR ingots. They have been examined with respect to the angle between the dendrite arms and axial planes, as seen in Figure 3.

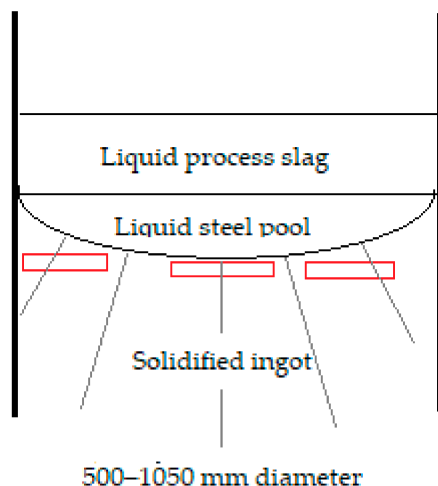


Figure 3. Schematic illustration of the longitudinal sections used for measuring the angle between the dendrites and the axial plane. Four samples were studied from the pressure electro-slag remelted ingots of 500 and 1050 mm diameter (PESR-500 and PESR-1050, respectively) and seven for the pressure electro-slag remelted ingot of 800 mm diameter (PESR-800).

Chemical compositions of the samples of the cross-sections were made using LECO CS600 (LECO Corporation, St. Joseph, MI, USA) for the element carbon (C) and sulfur (S) and X-ray Thermo 9800 for the other elements.

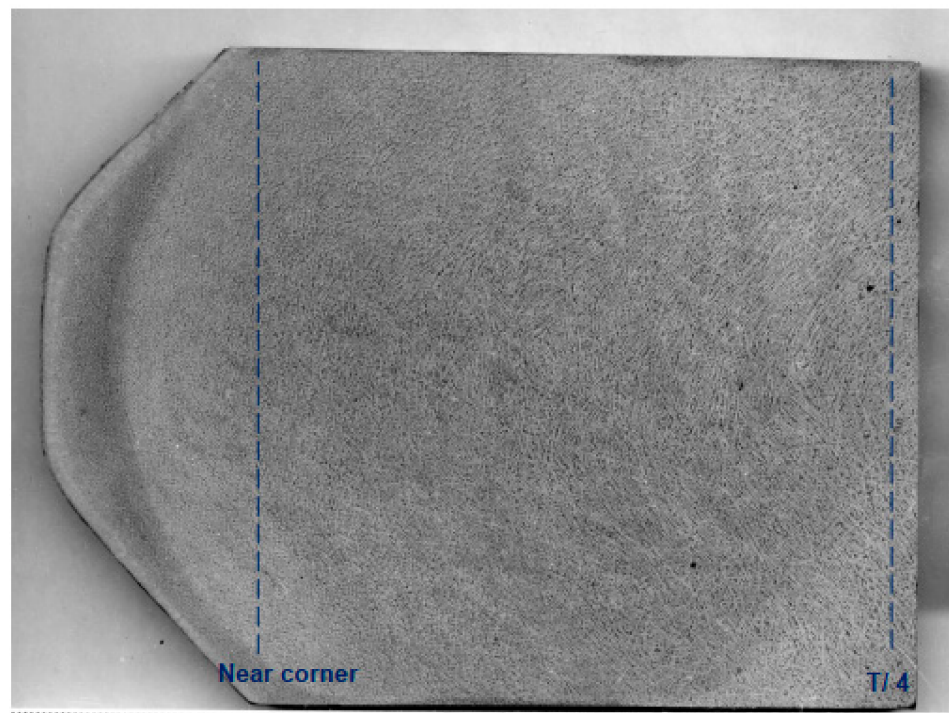
Both the SDAS at different positions and the angles between the dendrite arms and the axial plane were measured using a light optical microscope (LOM, Leica Microsystems, Wetzlar, Germany), Leica MZ6 equipped with Leica Qwin Runner V3.5.1 software. The investigations on the cross and longitudinal sections were made at former Exova AB, Karlskoga, Sweden.

Inclusion measurement were made on the cross-sections on the PESR-800 and PESR-1050 ingots. The field of view per sample was about 2000 mm². Inclusion measurements were been made on bottom, middle, and top samples on forged/rolled materials. The field of view per sample was about 6000 mm². Both the samples from the ingots and from the forged/rolled materials were studied using a scanning electron microscopy (FEI Quanta 600 Mark II, Thermo Fisher Scientific, Waltham, MA, USA). The number, size and, chemical composition of the inclusions larger than 8 µm were determined using the software Inca features from Oxford Instruments (ETAS Group, Stuttgart, Germany). Afterwards, the inclusions were divided into four size classes, namely, (i) 8–11.2 µm, (ii) 11.2–22.4 µm, (iii) 22.4–44.8 µm, and (iv) larger than 44.8 µm.

3. Results

3.1. Macrostructures of the Electrode and ESR/PESR Ingots

The macrostructure of the electrodes cross-sections at radial bottom, middle, and top positions is analyzed from the cross-section samples. The electrode was cast with the “big end down.” The macrostructure of the ESR ingot cross-section at two axial positions and the PESR ingots at the axial middle section was studied. No clear surface columnar zone could be observed in the radial ESR or PESR samples as shown in Figure 4a–c. The columnar zone in the electrode measured from the corner was found to be approximately 60 mm for the cross-sections from the radial bottom, see Figure 4d, 40 mm for the radial middle, and 90 mm for the radial top positions.



(a)

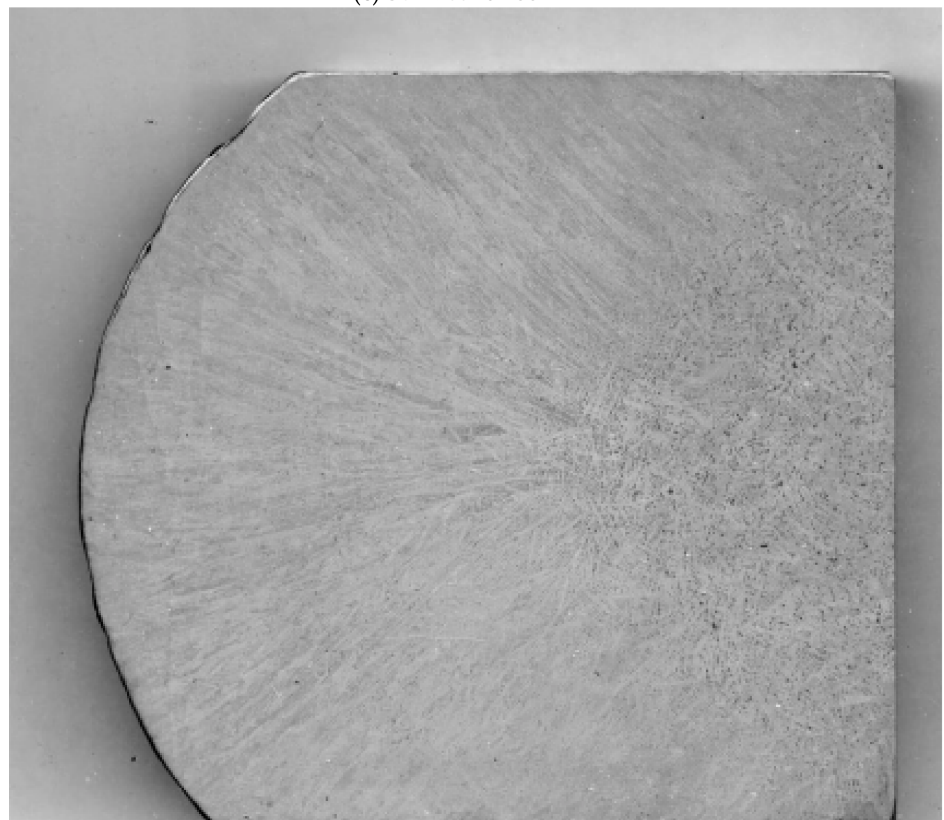


(b)

Figure 4. Cont.



(c) Surface to 155 mm.



(d) Surface to 155 mm.

Figure 4. Examples of the macrostructures in the electrode and the ingots. (a) Electro-slag remelted $400 \times 400 \text{ mm}^2$ ingot (ESR-400), from surface to position T/4 (in between corner and center). (b) Pressure electro-slag remelted 500 mm diameter ingot (PESR-500) with position T/6 (in between corner and position T/4) and position T/4 marked. The arrows point at the etching concentric bands. (c) Pressure electro-slag remelted 1050 mm diameter ingot (PESR-1050) from surface to 155 mm. The arrows point at the etching concentric bands. (d) Electrode $300 \times 300 \text{ mm}^2$ (CE-300) from surface to 155 mm.

A coarser dendritic pattern can be seen starting from 80 to 90 mm from the surface on the PESR-500 and 100 to 110 mm from the surface on the PESR-1050, see Figure 4b,c. Furthermore, white etching concentric bands are weakly visible at a distance approximately 15–30 mm below the surface for the samples PESR-500, -800, and -1050, see Figure 4b,c.

3.2. Dendrite Arm Spacing of the Electrode and ESR/PESR Ingots

The secondary dendrite arm spacing (SDAS) was measured on the cross-sections of the electrode and the ESR and PESR ingots. The measurement positions are shown in Table 2, the measurement principle is shown in Figure 5, which shows the primary arms, and their connecting secondary arms are marked in red. The measurements were made in-between the red secondary arms. Two to four measurements on each position were used to determine an average SDAS value per position.

Table 2. Secondary dendrite arm spacing (SDAS, λ_2) per distance from the surface for the electrode $300 \times 300 \text{ mm}^2$ (CE-300), the electro-slag remelted ingots $400 \times 400 \text{ mm}^2$ (ESR-400 1,2), and the pressure electro-slag remelted ingots with 500–1050 mm diameter (PESR-500, PESR-800, and PESR-1050).

Distance from Surface (mm)	SDAS, λ_2 (μm) per Electrode and Ingot Type (mm)					
	CE-300	ESR-400 1	ESR-400 2	PESR-500	PESR-800	PESR-1050
0						
30	159					
33		162	173			
44					226	
83				287		
75	232					
136		222	229		267	
123				306		
150	268					
171						488
202		274	280		409	
249				397		
257						788
395					569	
510						847
R^2 linjär	0.8907	0.9929	0.9903	0.995	0.9591	0.6368
R^2 polynom						1

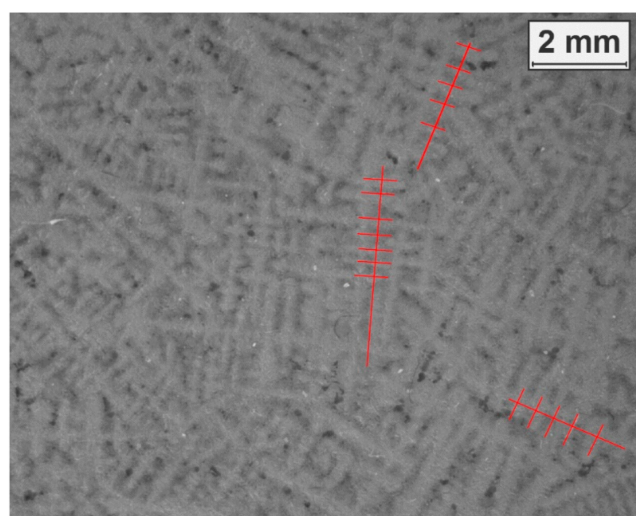


Figure 5. Measure principle, example from position T/2 (center) of the 500 mm in diameter ingot (PESR-500). The primary arms and their connecting secondary arms are marked in red. The measurement was made in-between the red secondary arms.

Difficulties in resolving the fine surface structure (except for the PESR-800) resulted in measurements of secondary arm spacing (SDAS) made at position T/6 (\approx quarter radius, near corner), instead of at the surface, as seen in Table 2 and Figure 6, in which the SDAS versus the axial positions on the electrode and the ingots are displayed. The curve for the PESR-1050 deviates from the other curves. The data and statistics for the SDAS measurements are shown in Table 3. The SDAS value per ingot and measured distance from the surface (mm) are displayed in Figure 7. It can be seen that the relation is approximately linear for the smaller ingots but more polygonal for the PESR-1050. The data behind Figure 7 is shown in Tables 2 and 3.

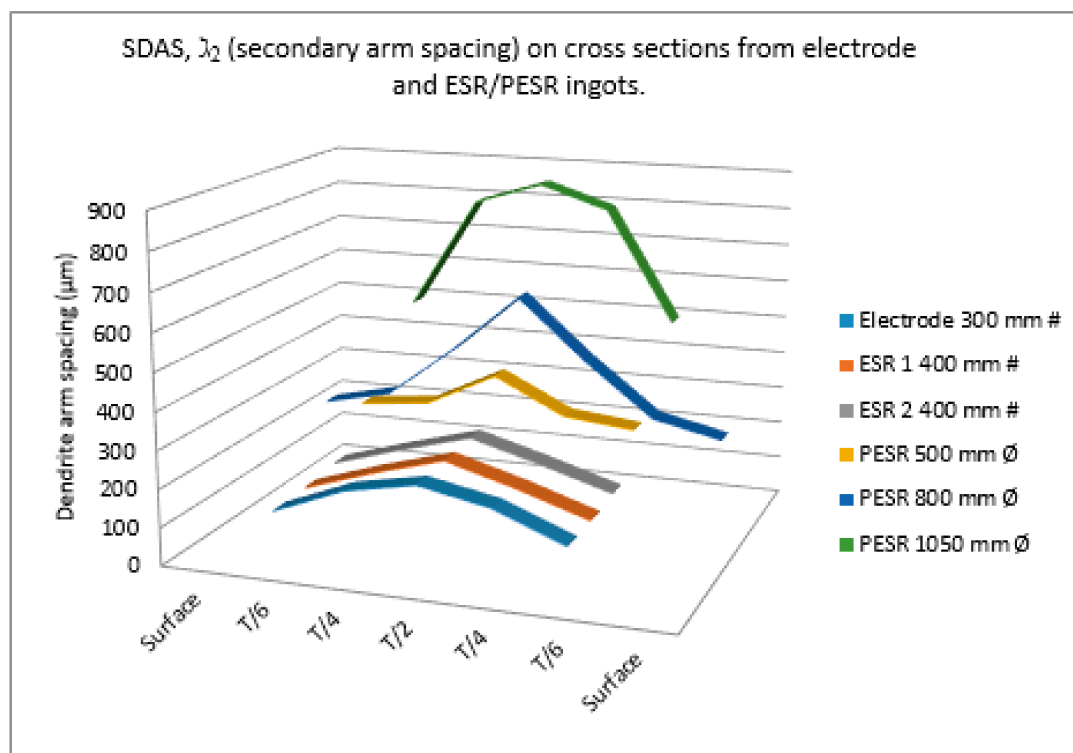


Figure 6. Secondary dendrite arm spacing, (SDAS, λ_2), (μm), for electrode $300 \times 300 \text{ mm}^2$ (C-300), electro-slag remelted $400 \times 400 \text{ mm}^2$ (ESR-400), and electro-slag remelted under pressure-controlled atmosphere pressure electro-slag remelted ingots 500–1050 mm in diameter (PESR-500, -800, and -1050). Cross-section positions: T/6—quarter radius, T/4—half radius, and T/2—center.

Table 3. Data and statistics for the secondary arm spacing, (SDAS, λ_2), measurements for electrode $300 \times 300 \text{ mm}^2$ (CE-300), the electro-slag remelted ingots $400 \times 400 \text{ mm}^2$ (ESR-400 1,2), and the pressure electro-slag remelted ingots 500–1050 mm in diameter (PESR-500, PESR-800, and PESR-1050).

Electrode/Ingot	Position	SDAS, λ_2 (μm)	Stdev (μm)	95% CI (μm)	% RA (%)	Measurements (no)
CE-300	Near corner	159	38	8	5	88
	T/4	232	61	13	5	90
	T/2	268	65	13	5	89
ESR-400 1	Near corner	162	55	11	7	88
	T/4	222	66	14	6	91
	T/2	276	70	15	5	88
ESR-400 2	Near corner	173	47	10	6	82
	T/4	229	68	14	6	88
	T/2	280	70	15	5	81
PESR-500	T/6	287	74	17	6	70
	T/4	306	104	24	7.8	73
	T/2	397	124	27	6.8	82

Table 3. Cont.

Electrode/Ingot	Position	SDAS, λ_2 (μm)	Stdev (μm)	95% CI (μm)	% RA (%)	Measurements (no)
PESR-800	Surface	226	62	14	6	76
	T/6	267	75	17	6	76
	T/4	409	148	30	7	91
	T/2	569	199	42	7	85
PESR-1050	T/6	488	142	28	5.7	101
	T/4	788	218	44	5.6	94
	T/2	847	213	41	4.9	101

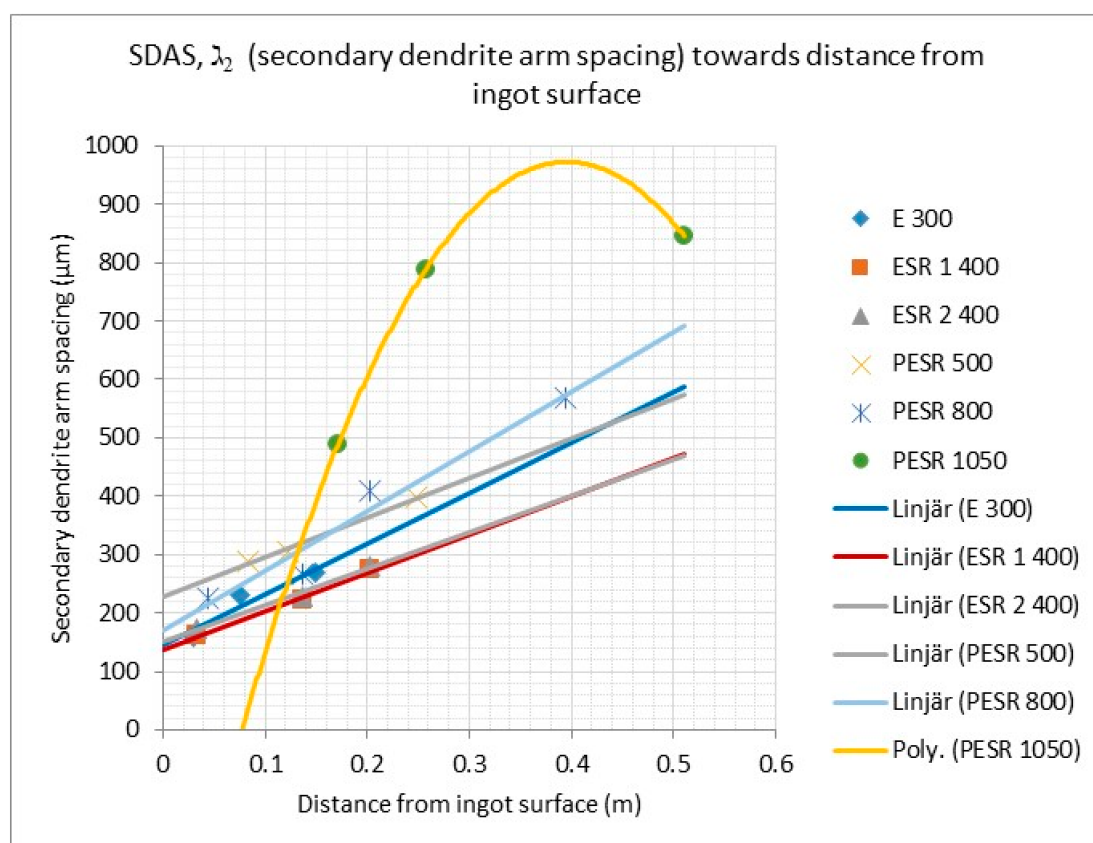


Figure 7. Secondary dendrite arm spacing, (SDAS, λ_2), per distance from surface for different ingot $300 \times 300 \text{ mm}^2$ (CE-300), the electro-slag remelted ingots $400 \times 400 \text{ mm}^2$ (ESR-400 1,2), and the pressure electro-slag remelted ingots 500–1050 mm in diameter (PESR-500, PESR-800, and PESR-1050).

3.3. Dendrite Arm Angles towards the Cross-Section of the Ingot

Longitudinal sections were cut from the cross-sections of three PESR ingots. The samples have been examined with respect to the angle between the dendrite arms and axial plane. The angles between dendrite arms and axial plane are shown in Table 4. The angle between the dendrite arm and the axial plane for the PESR-500 and PESR-800 is exactly 90° in position T/2, at the center of the ingot. For the PESR-1050, the angle could not be measured at T/2, as the macrostructure had no distinct direction at this position. According to theory [30,31,34], the angle of the dendrites towards the bottom of the liquid steel pool is 90° . This is valid as long as the solidification results in a columnar-dendritic structure. However, if the solidification results in an equiaxial structure, no distinct direction of the dendrites exists.

Table 4. Data and statistics for the angle between the dendrite arms and the axial plane. Electrode $300 \times 300 \text{ mm}^2$ (CE-300), the electro-slag remelted ingots $400 \times 400 \text{ mm}^2$ (ESR-400 1,2), and the pressure electro-slag remelted ingots 500–1050 mm in diameter (PESR-500, PESR-800, and PESR-1050).

Electrode	Position	Angle 1 (°)	Angle 2 (°)	Angle 3 (°)	Angle 4 (°)	Average (°)
PESR-500	Surface	52.4		57		54.7
	T/6	65.5		66.1		66
	T/4	72.2		71.8		72
	T/2	90		90		90
PESR-800	Surface	45	51.7	58.5	52.2	51.9
	T/6	69.8	72	65.5	73.3	70.2
	T/4	60	58.4	54.3	65.1	59.5
	T/2	90				90
	T/4	66.1	62.6	62.2	62.5	63.3
	T/6	72.5	77.9	72.2	72.5	73.8
PESR-1050	Surface	44	39.5	40.6	40.2	41.1
	Surface	38.2	45.6	51.8	58.8	48.6
	T/6	73.7	73.9	65.4	67	70
	T/4	65.8	72.6	72.5	68	69.7
	T/2	could not be determined				

Pictures of the measured angles for the PESR-800 and PESR-1050 are shown in Figure 8a,b. It can clearly be seen that the angle in the center is 90° for PESR-800 and that no angle could be measured for the PESR-1050.

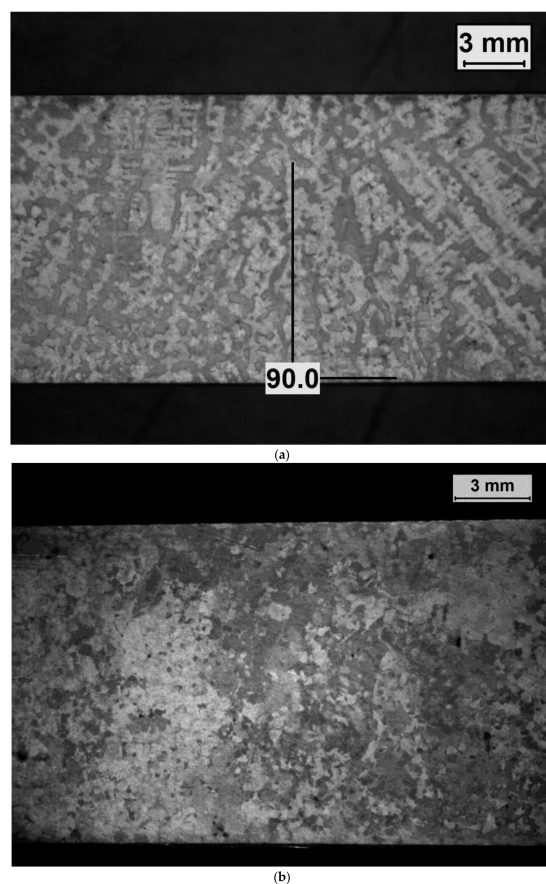
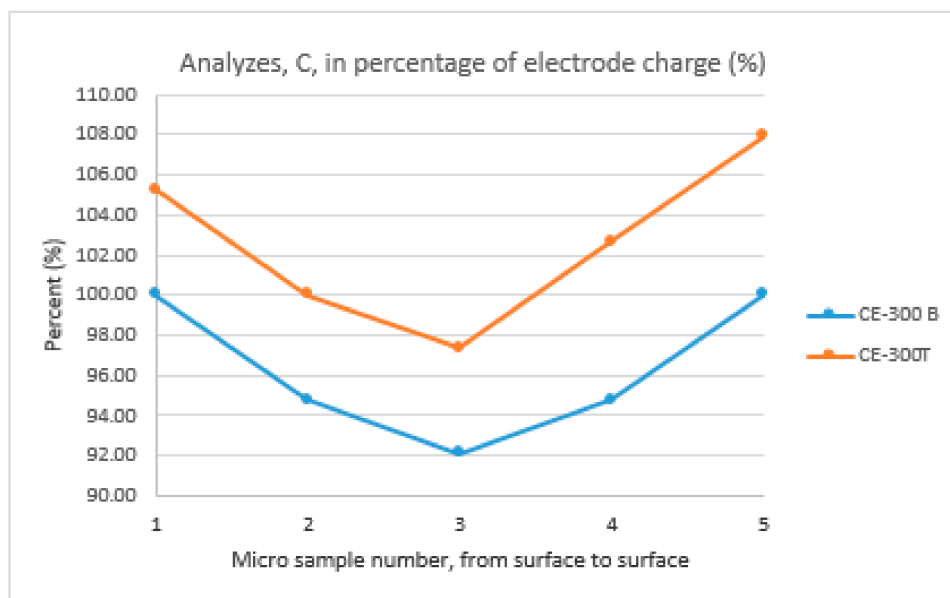


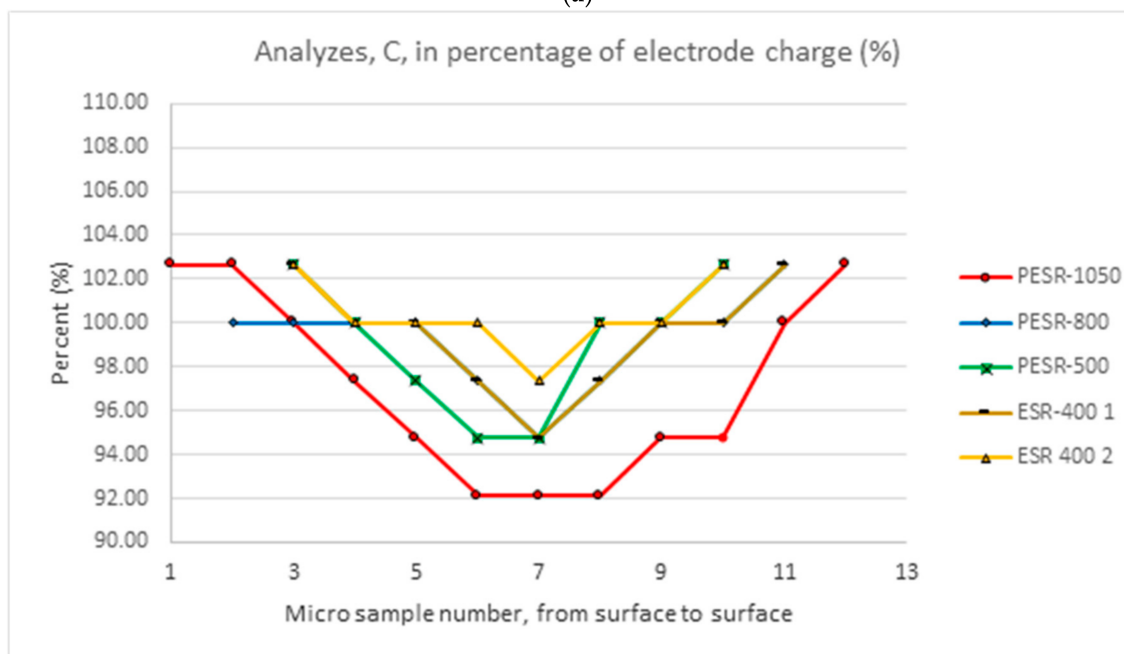
Figure 8. (a) Angle between the dendrite arms and the axial plane at position T/2 on the pressure electro-slag remelted 800 mm in diameter ingot (PESR-800). (b) The angle between the dendrite arms and the axial plane was not determined at position T/2 on the pressure electro-slag remelted (PESR) 1050 mm in diameter ingot.

3.4. Chemical Compositions over the Cross-Sections

The deviations between the amount of carbon (C) in the electrode and ingots and their electrode charge are displayed in Figure 9a,b. The radial segregation of the element C between the top and bottom sample of the electrode, as well as the larger axial segregation in the larger relative to the smaller ingots, can be seen clearly. The axial segregation of carbon in the ESR and PESR ingots is larger as the larger ingot diameter increases.



(a)



(b)

Figure 9. (a) The deviations between the amount of carbon (C) at bottom (B) and top (T) of the electrode $300 \times 300 \text{ mm}^2$ (C-300) and the corresponding electrode charge. (b) The deviations between the amount of carbon (C) in the ingots and their corresponding electrode charges. Electro-slag remelted ingot $400 \times 400 \text{ mm}^2$ and pressure electro-slag remelted ingots 500–1050 mm in diameter (PESR-500, PESR-800, and PESR-1050).

The amount of sulfur (S) in the remelted ingots is approximately 25% of the amount in their corresponding electrode charges. The amounts of manganese (Mn), chromium (Cr), and vanadium, (V) are relatively stable compared to the amounts in their corresponding electrode charges. However, the elements Cr and Mn can have a slight decrease in the axial center of the larger ingots. Silicon is 0–5% lower in the remelted ingots compared with the corresponding electrode charges. This decrease is due to the reaction with the ESR or PESR process slag.

3.5. Number of Oxide Inclusions per Size, Position, and Ingot Type

The number of oxide inclusions per size class and ingot type from the electrode and the rolled/forged and heat-treated material (after approximately 75% reduction) at different axial positions is displayed in Figure 10. The samples are taken at position T/2, at the center of the ingot. The ingots used in this investigation are the same as in the solidification structure samples, supplemented with results from a 650 mm in diameter ingot. The ESR-400 mm and the PESR-500Ø ingots are from the same electrode charge from the steel shop. Normally, the number of inclusions increase almost linear with the ingot size, specifically when a larger statistical basis is studied. No inclusions > 44.8 µm were detected in the processed material.

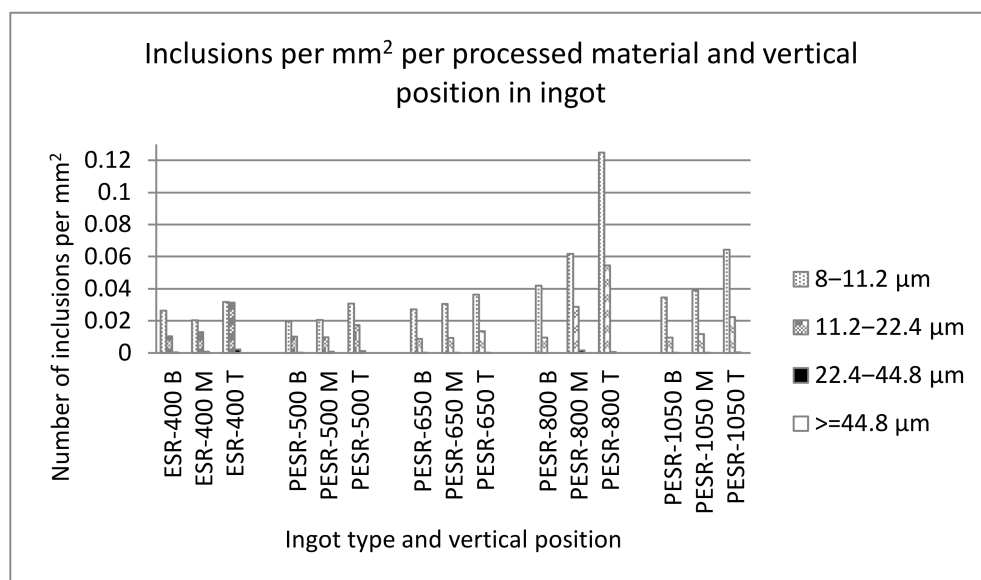


Figure 10. Number of oxide inclusions per mm² and ingot size and from the electrode and the processed material from the ingots (after approximately a 75% reduction) at different axial positions. Electro-slag remelted ingot 400 × 400 mm² (ESR-400) and pressure electro-slag remelted ingots 500–1050 mm in diameter (PESR-500, PESR-650, PESR-800, and PESR-1050) at bottom (B), middle (M), and top (T) positions. No inclusions > 44.8 µm were detected in the processed material.

The number of oxide inclusions per size class and ingot position measured in percentage of the largest number of inclusions per size class, measured over the cross-section for the unprocessed ingot types PESR-800 and PESR-1050, is displayed in Figure 11. It can be seen that the numbers of inclusions increase with distance from the surface. In laboratory and/or pilot scale, this phenomenon may be neglected. No inclusions > 44.8 µm were detected in the ingots.

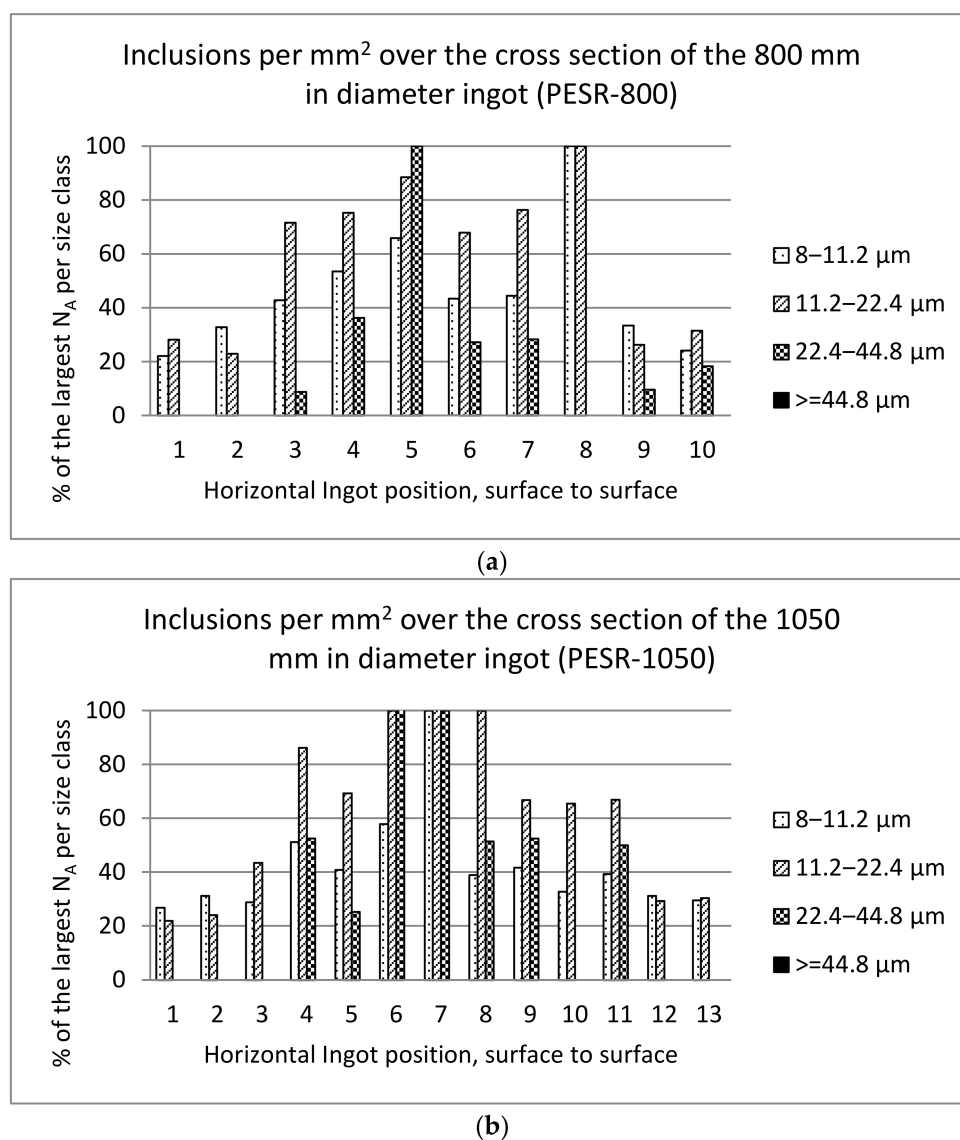


Figure 11. Inclusion measurement over the cross-sections for the pressure electro-slag remelted (a) 800 mm diameter (PESR-800) and (b) 1050 mm diameter (PESR-1050) unprocessed ingots. No inclusions > 44.8 μm were detected.

3.6. Inclusion Composition

The most common inclusion types in the size range of 8–44.80 μm in the electrode are almost pure MnS inclusions followed by almost pure Al₂O₃ and Al₂O₃–CaO oxides containing <10% MgO. For the ESR ingot, Al₂O₃ and Al₂O₃–CaO oxides followed by Al₂O₃–CaO–MgO oxides are the most common inclusions. For the PESR-ingots, Al₂O₃–CaO–MgO oxides followed by Al₂O₃ and Al₂O₃–CaO oxides, are the most common inclusions. The difference between ESR and PESR remelted ingots are probably mostly due to the continuous Al de-oxidation during ESR remelting in air [27].

4. Discussion

4.1. Solidification

The solidification of an ingot either starts with a surface zone with small equiaxial dendrites or long radially orientated crystals [34]. At a certain distance from the mould when the cooling is smaller, the columnar dendritic structure (CD) appears. The reason for that no clear visible columnar zone was found on the ESR and PESR samples is that remelted ingots solidify with a dendrite angle of 90° towards the bottom of the liquid

pool unlike the conventional cast electrode that solidifies with a dendrite angle slightly above 90° towards the top center. The larger equiaxial structure in the center were only found in the CE-300 and the PESR-1500. This is due to their higher Longest Solidification Time (LST).

The relationship between the dendrite arm distance and the growth rate can be described as follows

$$U_{\text{growth}} \times \lambda_{\text{den}}^2 = C, \quad (1)$$

where U_{growth} is the growth rate, λ_{den} is the distance between the secondary or primary dendrite arms, and C is a constant [30]. It is established that the constant is $10^{-6} \text{ cm}^3/\text{s}$ for low carbon iron base alloys and that it should (information given to the author by Professor Emeritus Hasse Fredriksson) be about the same for this steel grade, as seen in Figure 12 and Table 5. It can be established that the growth rates for the ingots that solidify entirely as columnar-dendritic structure correlates best with a linear equation, as seen in Equation (1). However, the PESR-1050 mm ingot, which has an equiaxial solidification structure in the center, correlates, according to the results in this investigation, more with a polygonal equation. The reason for that is that Equation (1) only is valid for the columnar dendritic zone and that it, therefore, should not be used for the equiaxial zone.

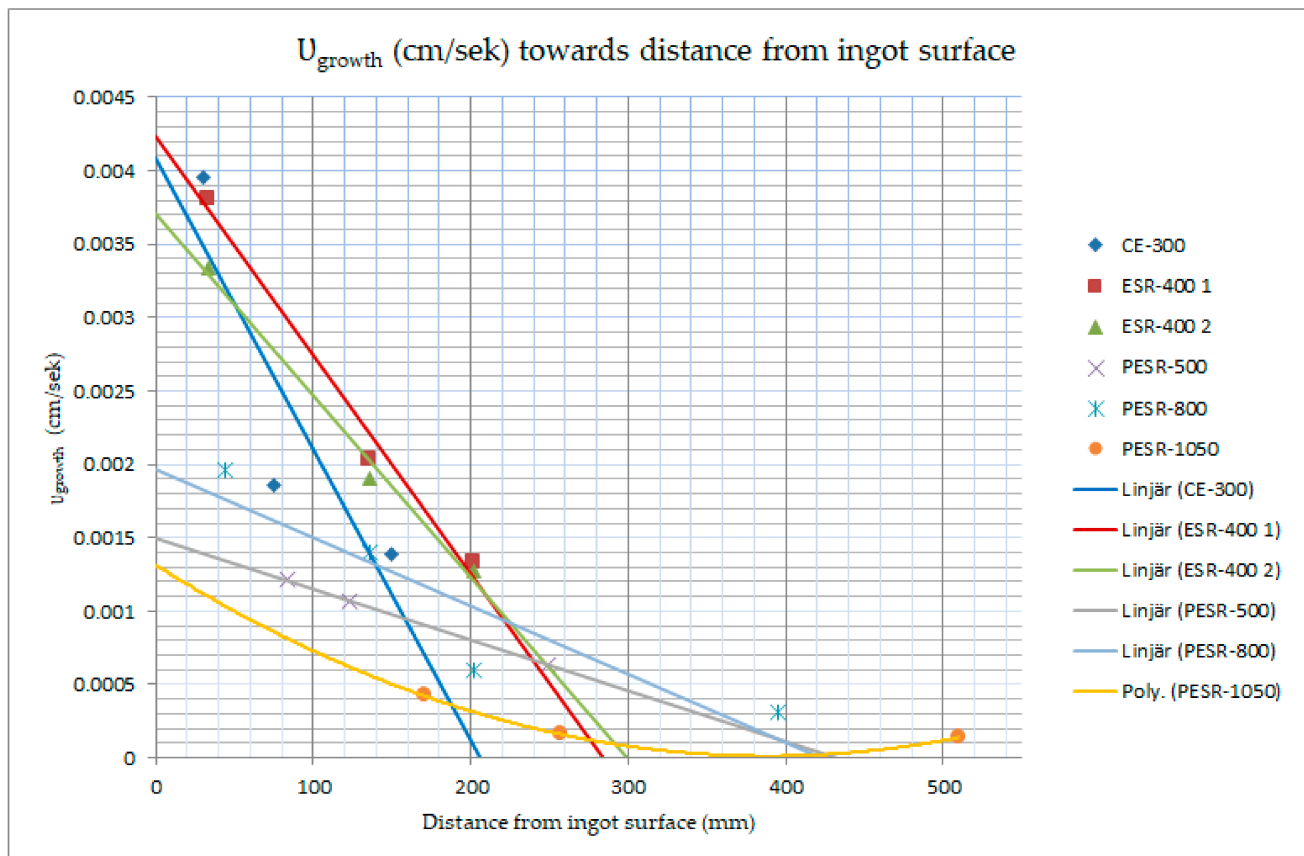


Figure 12. Growth rate towards distance from ingot surface. Equation (1) is just valid for columnar dendritic growth, the nonlinear connection for the pressure electro-slag remelted 1050 mm in diameter ingot (PESR-1050) indicates that it solidifies equiaxial in the center.

Table 5. Distance from ingot surface (mm) and growth rate, U_{growth} (m/s), per electrode $300 \times 300 \text{ mm}^2$ (CE-300), electro-slag remelted ingot (ESR-400), and pressure electro-slag remelted ingots 500–1050 mm in diameter (PESR-500, PESR-800, and PESR-1050).

Ingot/Growth Rate U_{growth} (m/s) per Position	Surface	T/6	T/4	T/2
CE-300		3.96×10^{-5}	1.86×10^{-5}	1.39×10^{-5}
ESR-400 1		3.81×10^{-5}	2.03×10^{-5}	1.33×10^{-5}
ESR-400 2		3.34×10^{-5}	1.91×10^{-5}	1.28×10^{-5}
PESR-500		1.21×10^{-5}	1.07×10^{-5}	6.34×10^{-6}
PESR-800	1.96×10^{-5}	1.40×10^{-5}	5.98×10^{-6}	3.09×10^{-6}
PESR-1050		4.20×10^{-6}	1.61×10^{-6}	1.39×10^{-6}

According to Imagumbai [39], the relation between the growth rate of the primary dendrite tip (R) and the temperature gradient around the solid/liquid tip (G) correlates to the primary dendrite spacing (λ_1), which can be expressed using the following relationship:

$$\lambda_1 [\mu\text{m}] = 1750 \times R^{-0.14} \times G^{-0.50} \quad [R: \mu\text{m/s}, G: ^\circ\text{C/mm}]. \quad (2)$$

Imagumbai [39] estimated the secondary dendritic arm spacing at a completely solidified zone (λ_2) to be approximately half of the primary dendritic arm spacing in an unidirectionally solidified C-Mn steel at steady state.

$$\lambda_2 \sim 0.5 \times \lambda_1. \quad (3)$$

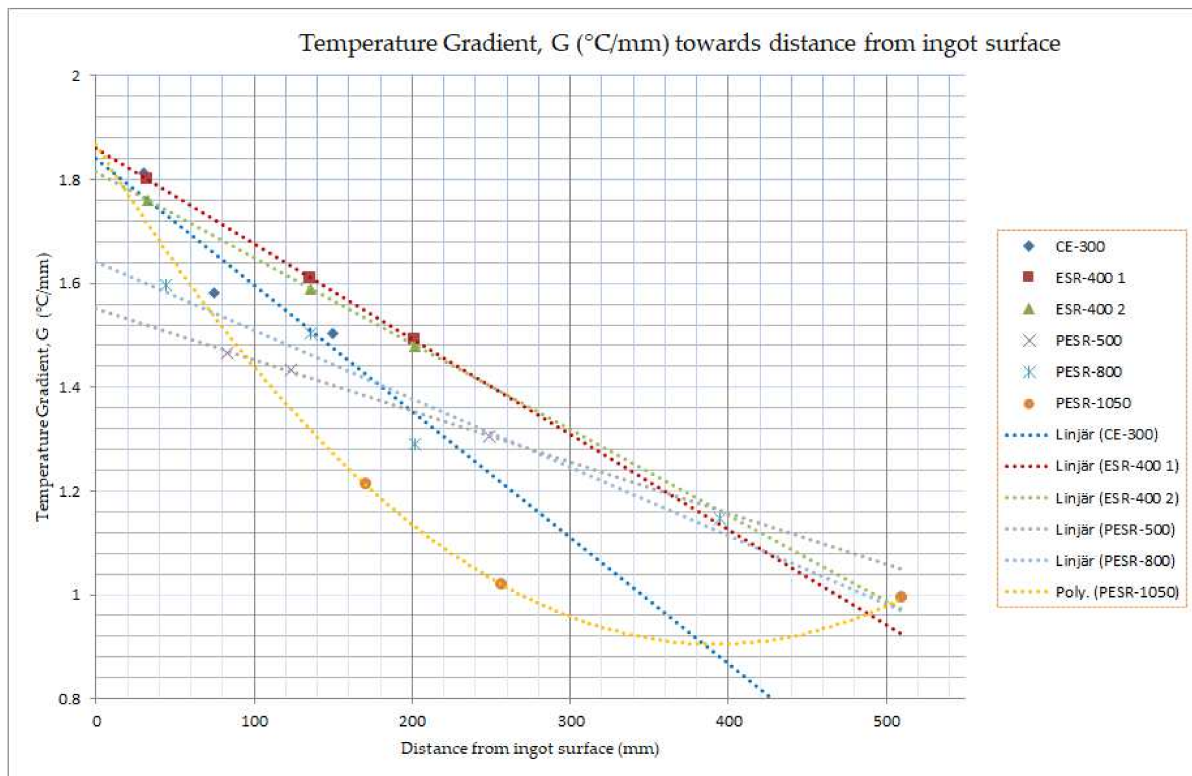
In Table 6 and Figure 13a, the temperature gradient is calculated by combining Equations (2) and (3) to give Equation (4).

$$G [^\circ\text{C/mm}] = \sqrt{(1750 \times R^{-0.14} / \lambda_1)}. \quad (4)$$

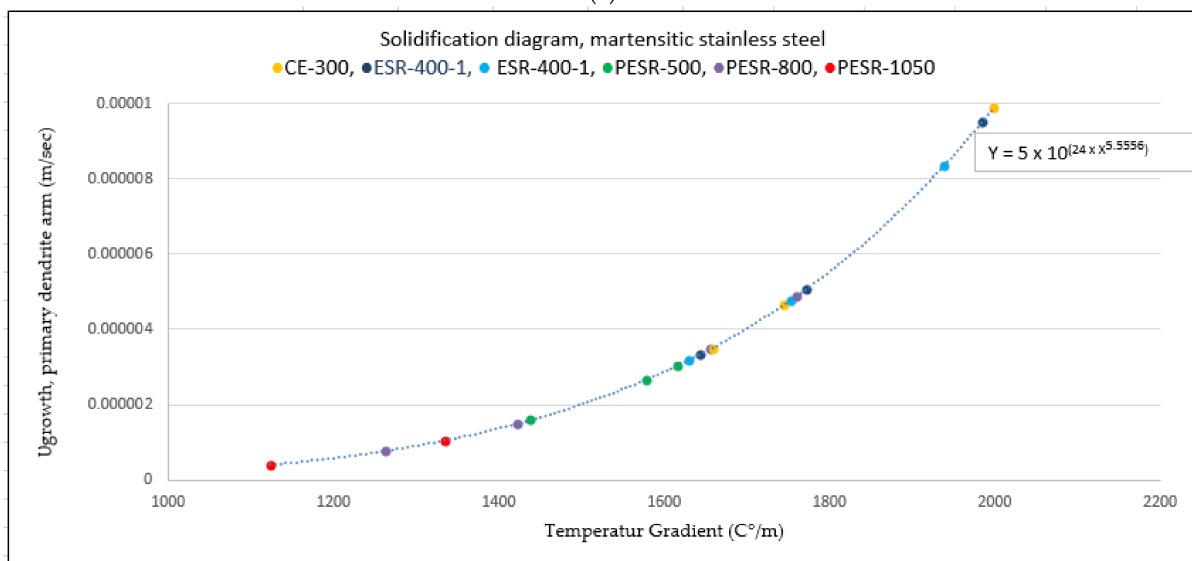
The figure shows that the PESR-1050 deviate from a linear relationship, which is due to the equiaxial solidification, structure in the center of the ingot. The growth rate (m/s) is plotted as a function of the temperature gradient ($^\circ\text{C/m}$), and its correlation is shown in Figure 13b (the result for position T2 for the PESR-1050 is excluded). The primary arms growth rate needed for the CET transition is less than $4 \times 10^{-7} \text{ m/s}$. In order to undertake the transition, the temperature gradient needs to be lower than approximately $10^3 \text{ }^\circ\text{C/m}$.

Table 6. Temperature gradient ($^\circ\text{C/mm}$) and distance from surface (mm) for electrode $300 \times 300 \text{ mm}^2$ (CE-300), electro-slag remelted ingot $400 \times 400 \text{ mm}^2$ (ESR-400), and pressure electro-slag remelted ingots 500–1050 mm in diameter (PESR-500, PESR-800, and PESR-1050).

Ingot/Temperature Gradient, G ($^\circ\text{C/m}$)	Surface	T/6	T/4	T/2
Electrode 300 mm #		1998.229	1744.105	1655.845
ESR 1 400 mm #		1984.828	1771.99	1642.699
ESR 2 400 mm #		1938.437	1752.296	1629.939
PESR 500 mm Ø		1615.514	1578.66	1437.42
PESR 800 mm Ø	1760.6344	1658.075	1422.092	1262.722
PESR 1050 mm Ø		1334.495	1123.049	1094.234



(a)



(b)

Figure 13. (a) Temperature gradient, G ($^{\circ}\text{C}/\text{mm}$), towards distance from ingot surface. Equation (1) (which also is used to calculate the temperature gradient) is just valid for columnar dendritic growth, the nonlinear connection for the pressure electro-slag remelted 1050 mm in diameter ingot (PESR-1050) indicates that it solidifies equiaxial in the center. (b) Growth rate, U_{growth} (m/s), towards temperature gradient, G ($^{\circ}\text{C}/\text{m}$).

Figure 14 displays data from the electrode and ingots (center position) in this investigation together with plotted data from Kurz solidification diagram [40]. The figure shows the growth rate U_{growth} (m/s) (calculated on primary dendrite arm spacings) vs. the temperature gradient G ($^{\circ}\text{C}/\text{m}$). According to Kurz [40], the area above the black curve solidifies in an equiaxial manner and the area below the line solidifies in a columnar-dendritic manner. The red dots for the electrode (CE-300) and the 10.500 mm ingot (PESR-1050) indicates

that they both solidify in an equiaxial manner and that the used Equation (1) is not valid for them.

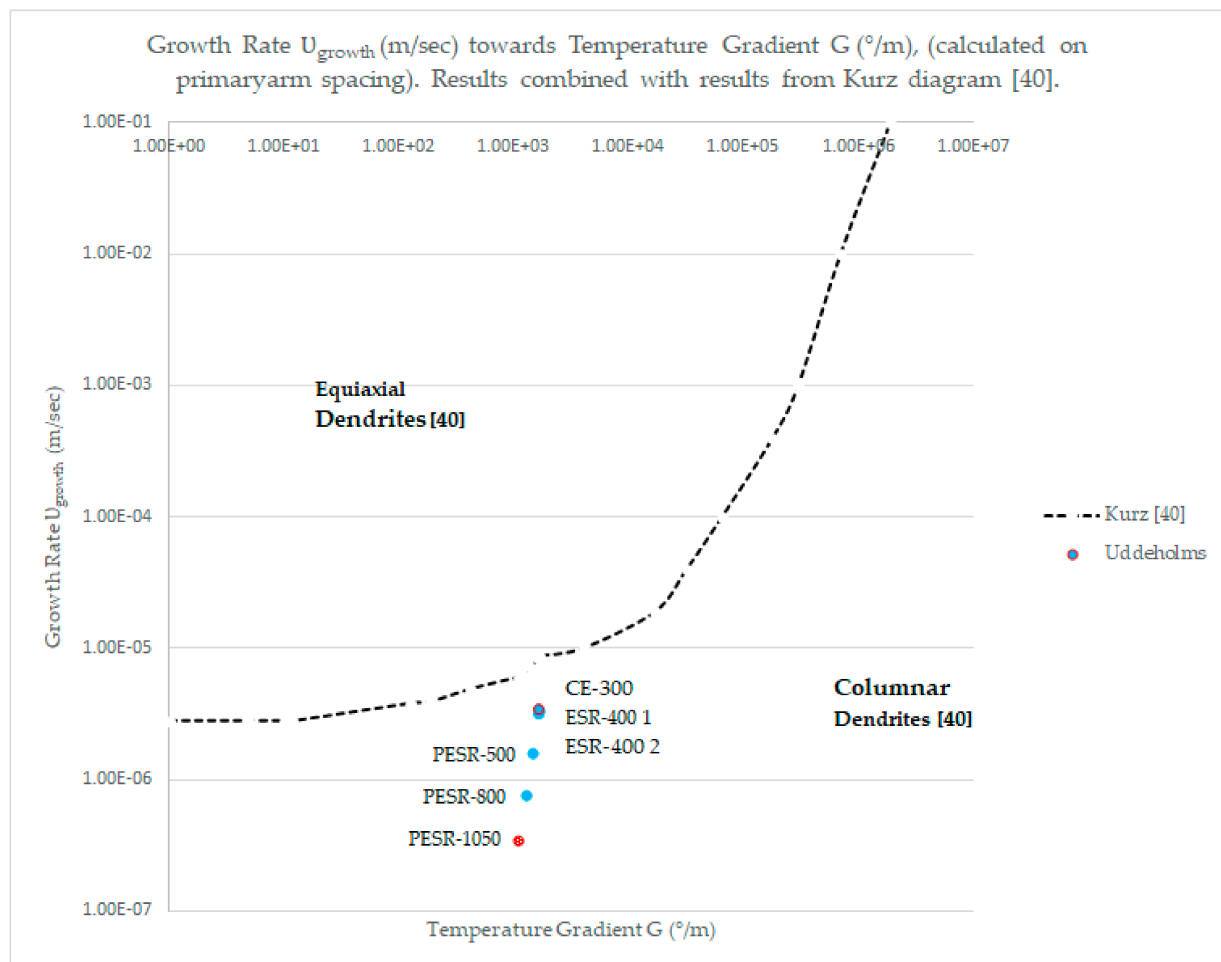


Figure 14. Growth rate U_{growth} (m/s) (calculated on primary dendrite arm spacings) versus the temperature gradient G ($^{\circ}\text{C}/\text{m}$) around the solid/liquid tip. The black line is plotted data from Kurz solidification diagram [40]. The area above the line solidifies in an equiaxial manner and the area below solidifies in a columnar-dendritic manner [40]. Data from Uddeholms martensitic stainless steel are included, the electrode $300 \times 300 \text{ mm}^2$, (CE-300), the electro-slag remelted ingots $400 \times 400 \text{ mm}^2$, (ESR-400), and the pressure electro-slag remelted ingots 500–1050 mm in diameter, (PESR-500, PESR-800, and PESR-1050). All data are from the center position of the ingots. The electrode and the PESR-1050, which solidify equiaxial dendritic in the center, are marked (\bullet), because the equations used are not valid for the equiaxial solidification structure.

4.2. Chemical Analyzes over the Cross-Sections

The axial segregations of C correspond to both the measured SDAS values and the dendrites orientations towards the bottom of the liquid pool. The more the C segregation, the larger the SDAS value and the larger the orientation angle. The reason is that both the segregation and the size of the SDAS and orientation angle correspond with the Longest Solidification Time (LST) which increases towards the center of the ingot. C is an interstitial element and will, therefore, segregate more than the more stable elements, like Cr and Mo. The decrease in the elements S and Si is due to reactions with the process slag.

4.3. Number of Oxide Inclusions per Size, Position, and Ingot Type

In a previous investigation, Sjöqvist Persson et al. [21] found that the difference in inclusion morphologies between different ESR/PESR ingot sizes was larger than the difference between the electrode heats. The tool steel grade contains a relatively high

amount of silica. Silica has a strong affinity to oxygen, which contributes to the de-oxidation process during ladle refining. This reaction results in a stable dissolved oxygen content in the electrode heats. Therefore, it is appropriate to compare the small ingots from the same electrode heat with the larger ingots from different electrode heats.

As expected (except the 800Ø mm ingot in this investigation), both this and the previous investigation [21] showed that larger ESR and PESR ingots contained a higher number of inclusions than the smaller ingots. This corresponds to the former universal theory that the majority of inclusions in an ESR or PESR ingot are secondary in nature and that they are formed due to slag/metal and de-oxidation reactions [9,21–25,29]. The larger the LST, the longer the time for the inclusions to precipitate and grow. This finding is further supported by the presence of a large number of small inclusions that presumably were precipitated during solidification. However, Sjöqvist Persson et al. [26,27] stated that the inclusions in a remelted ingot can both be primary, semi-secondary, or secondary inclusions. The result also corresponds to the new theory, since even the semi-secondary inclusions will have a longer time to grow. Furthermore, the primary inclusion maybe more numerous due to the probable differences in the liquid film formation on the electrode's melting surface.

Previous investigations have shown that the amount of larger inclusions (22.4–44.8 µm) is higher for the 1050 mm in diameter ingot (PESR-1050) than for the smaller PESR ingots. In order to improve the statistical accuracy, the results from the previous presented investigation [21], unpublished results from six PESR-1050, and the new results from this investigation are put together in Figure 15. As seen in the picture, the number of the larger inclusions (22.4–44.8 µm) is nearly doubled from the PESR-800 to the PESR-1050 ingots. This result demonstrates that the relation between the amount of larger inclusions (here 22.4–44.8 µm) in different ingot sizes is strongly related to whether or not the material has solidified with a columnar-dendritic or equiaxial structure. The PESR-1050 ingot is no longer in production use for this steel grade.

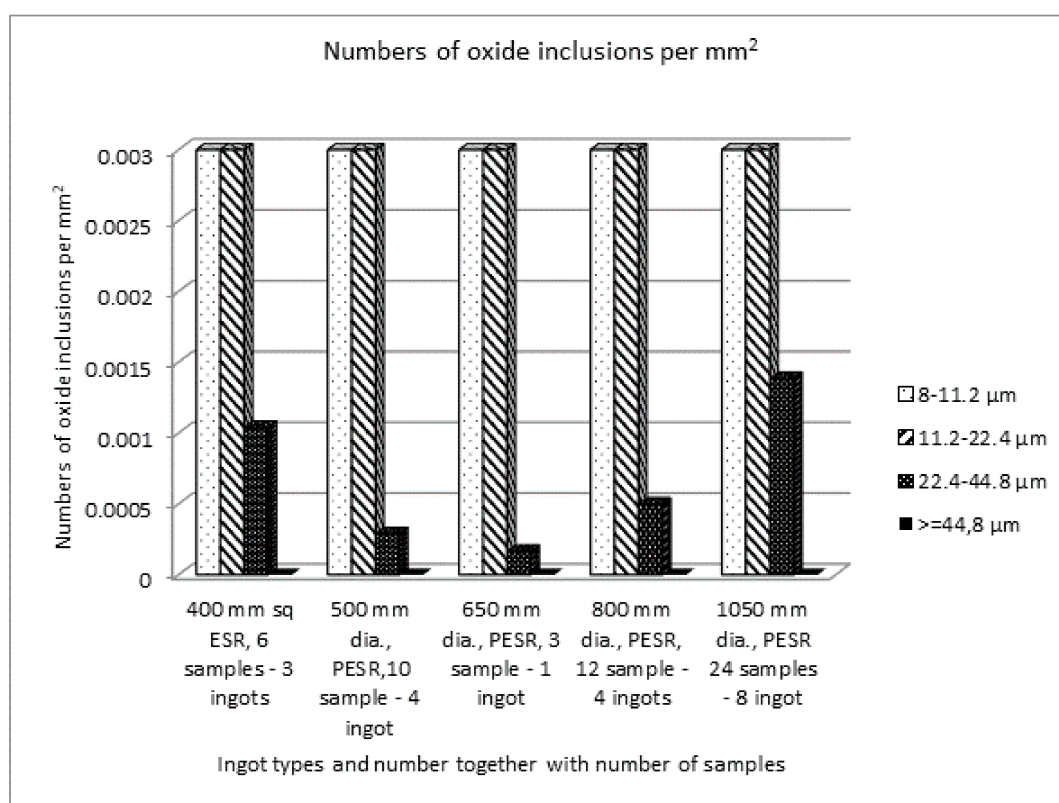


Figure 15. Number of oxide inclusions per mm², for different ingot sizes from rolled/forged and heat-treated material. No inclusions > 44.8 µm were detected.

5. Conclusions

The focus of the study was the impact of the solidification on the inclusion morphologies in different sizes of electro-slag, (ESR) and pressure electro-slag, (PESR) remelted ingots in a common martensitic steel grade. The inclusion characteristics were studied using LOM and SEM. The main conclusions may be summarized as follows:

- The transition between a dendritic and an equiaxial solidification in the center of the ingots in this steel grade takes place in the region between the ingot diameters of 800 and 1050 mm. The primary arms growth rate needed for the CET transition is less than 4×10^{-7} m/s. In order to undertake the transition, the temperature gradient must be less than approximately 10^3 °C/m.
- The transition can readily be seen by measuring the angle towards the surface on the side of cross-sections from the remelted ingots. Up to the ingot 800 mm in diameter, the dendritic growth direction in the center of the ingot is parallel to the ingot axis. In the case of the 1050 mm in diameter ingot, it was not possible to determine a dendrite growth direction in the center of the material.
- The axial segregations of carbon, (C), correspond both to the measured secondary dendritic arm spacing, (SDAS), values and the dendrites angles towards the bottom of the liquid pool. The more C segregation, the larger the SDAS value and the larger, (or no angle as for the PESR-1050), the angle.
- The larger the ingot and the further towards the center of an ingot, the larger the inclusion sizes. As long as an ingot solidifies with a columnar dendritic structure, the increase in the inclusion numbers and sizes for larger ingots are almost linear. However, at the ingot size (1050 mm in diameter in this study) when the center of the ingot solidifies in an equiaxial mode, the increase in number and size of the inclusions is much higher.
- The measurement of the amount of larger inclusions (here >22.8 µm) on different ingot sizes will give a good indication of where the transition from a dendritically to equiaxial solidification takes place.

Author Contributions: Conceptualization, E.S.P.; methodology, E.S.P. and S.B.; software and validation, E.S.P. and A.M.; formal analysis, E.S.P. and S.B.; investigation, E.S.P.; resources, E.S.P.; data curation, E.S.P.; writing—original draft preparation, E.S.P.; writing—review and editing, E.S.P., A.M. and P.G.J.; visualization, E.S.P.; supervision, A.M.; project administration, E.S.P.; funding acquisition, E.S.P. All authors have read and agreed to the published version of the manuscript.

Funding: This research received no external funding.

Institutional Review Board Statement: Not applicable.

Informed Consent Statement: Not applicable.

Acknowledgments: The author wish to thank Emeritus Hasse Fredriksson for fruitful discussions during the course of this work.

Conflicts of Interest: The authors declare no conflict of interest.

References

1. Stefanescu, D.M. Microstructure Evolution during the solidification of Steel. *ISIJ Int.* **2006**, *46*, 786. [[CrossRef](#)]
2. Kay, D.A.R.; Pomfret, R.J. Removal of inclusions during AC Electroslag remelting. *J. Iron Steel Inst.* **1971**, *209*, 962–965.
3. Li, Z.B.; Zhou, W.H.; Li, Y.D. Mechanism of removal on non-metallic inclusions in the ESR process. *Iron Steel* **1980**, *15*, 20–26.
4. Shi, C.; Chen, X.-C.; Guo, H.-J. Oxygen control and its effect on steel cleanliness during Electroslag remelting of NAK80 die steel. In Proceedings of the Iron and Steel Conference and Exposition AISTech 2012, Atlanta, GA, USA, 7–10 May 2012; pp. 947–957.
5. Shi, C.; Chen, X.-C.; Guo, H.-J.; Zhu, Z.-J.; Ren, H. Assessment of oxygen control and its effect on inclusion characteristics during ESR remelting of die steel. *Steel Res. Int.* **2012**, *83*, 472–486. [[CrossRef](#)]
6. Shi, C.; Chen, X.-C.; Guo, H.-J. Characteristics of inclusions in high-Al steel during electroslag remelting process. *Int. J. Miner. Mater.* **2012**, *19*, 295–302. [[CrossRef](#)]
7. Chen, X.C.; Shi, C.B.; Guo, H.J.; Wang, F.; Ren, H.; Feng, D. Investigations of oxide inclusions and primary carbon nitrides in Inconel 718 Superalloy refined through electroslag remelting process. *Metall. Mater. Trans. B* **2012**, *43*, 1596–1607. [[CrossRef](#)]

8. Burel, B.C. A Study of Inclusion Behavior during Electroslag Remelting. Ph.D. Thesis, University of British Columbia, Vancouver, BC, Canada, 1969.
9. Mitchell, A. Oxide inclusion behavior during consumable electrode remelting. *Ironmak. Steelmak.* **1974**, *1*, 172–179.
10. Chan, J.C.F.; Miller, J.W.G.D.; Cameron, J. The Re-resolution of Inclusions in Remelted Stainless Steels. *Metall. Mater. Trans. B* **1976**, *7B*, 135–141. [[CrossRef](#)]
11. Shi, C.; Chen, X.-C.; Luo, Y.-W.; Guo, H.-J. Theory analysis of steel cleanliness control during electroslag remelting. In *Materials Processing Fundamentals*; Springer: Cham, Switzerland, 2013.
12. Dong, Y.; Jiang, Z.; Cao, Y.; Fan, J.; Yu, A.; Liu, F. Effect on fluoride containing slag on oxide inclusions in electroslag ingot. In Proceedings of the Liquid Metal Processing & Casting Conference, Austin, TX, USA, 22–25 September 2013.
13. Dong, Y.-W.; Jiang, Z.-H.; Cao, Y.-L.; Hou, D. Effect of slag on Inclusions during electroslag remelting process of die steel. *Metall. Mater. Trans. B* **2014**, *45B*, 1315–1324. [[CrossRef](#)]
14. Shi, C.; Chen, X.-C.; Guo, H.-J.; Sun, X.L.; Zhu, Z.-J. Control of $\text{MgO} \cdot \text{Al}_2\text{O}_3$ spinel inclusions during protective gas electroslag remelting of die steel. *Metall. Mater. Trans. B* **2013**, *44B*, 378–389. [[CrossRef](#)]
15. Schneider, R.; Schuler, C.; Wurstinger, P.; Reiter, G.; Martinez, C. Einfluss eines höheren SiO_2 -Gehaltes in der Schlacke beim Umschmelzen eines Varmarbeitsstahles auf ESU-prozess. *Berg. Hüttenmännische* **2015**, *160*, 117–122. (In German) [[CrossRef](#)]
16. Shi, C.; Zhu, Q.-t.; Yu, W.-t.; Song, H.-d.; Li, J. Effect on oxide inclusions modification during electroslag remelting on primary carbides and toughness of a high-carbon 17% Cr tool steel. *J. Mater. Eng. Perform.* **2016**, *25*, 4785–4795. [[CrossRef](#)]
17. Du, G.; Li, J.; Wang, Z.-B. Effect on operating conditions on inclusion of Die Steel during Electroslag remelting. *ISIJ Int.* **2017**, *29*, 1–10.
18. Chang, L.Z.; Shi, X.F.; Cong, J.Q. Study on mechanism of oxygen increase and countermeasure to control oxygen content during electroslag remelting process. *Ironmak. Steelmak.* **2014**, *41*, 182–186. [[CrossRef](#)]
19. Shi, C.; Park, J.H. Evolution of Oxide inclusions in Si-killed Steel during Protective Atmosphere Electroslag remelting. *Metall. Mater. Trans. B* **2019**, *50B*, 1139–1147. [[CrossRef](#)]
20. Reiter, G.; Schuetzenhoefer, W.; Tazreiter, A.; Martinez, C.; Wurstinger, P.; Loecker, C. The influence of different melting and remelting routes in the cleanliness of high alloyed steels. In Proceedings of the Liquid Metal Processing & Casting conference LMPC 2013, Austin, TX, USA, 22–25 September 2013.
21. Persson, E.; Mitchell, A.; Fredriksson, H. The behavior of Inclusion during ESR remelting. In Proceedings of the 2nd Ingot Casting Rolling Forging Conference ICRF 2014, Stahleisen, Germany; Milan, Italy, 7–9 May 2014.
22. Persson, E.S.; Fredriksson, H.; Mitchell, A. Differences in inclusion morphology between ESR remelted and ingot casted common martensitic steel. In Proceedings of the 5th International Conference on Process Development in Iron and Steelmaking Scanmet-V 2016, Luleå, Sweden, 12–15 June 2016.
23. Wang, H.; Li, J.; Shi, C.B.; Li, J. Evolution of Al_2O_3 inclusions by magnesium treatment in H13 hot work die steel. *Ironmak. Steelmak.* **2017**, *44*, 128–133. [[CrossRef](#)]
24. Persson, E.S.; Karasev, A.; Jönsson, P.G. Studies of three dimension inclusions from ESR remelted and conventional cast steel. In Proceedings of the Liquid Metal Processing & Casting Conference LMPC, USA, TMS, Philadelphia, PA, USA, 10–13 September 2017.
25. Persson, E.S.; Mitchell, A. Differences in inclusion morphology between ESR remelted steel with and without tracer in the slag. In Proceedings of the Liquid Metal Processing & Casting Conference LMPC, USA, TMS, Philadelphia, PA, USA, 10–13 September 2017.
26. Persson, E.S.; Mitchell, A. The importance of Electrode Cleaness in the ESR/PESR Processes. In Proceedings of the 3rd Ingot Casting Rolling Forging conference ICRF, Stahleisen, Germany; Stockholm, Sweden, 16–19 October 2018.
27. Persson, E.S.; Karasev, A.; Mitchell, A.; Jönsson, P.G. Origin of the Inclusions in Production-Scale Electrodes, ESR Ingots, and PESR Ingots in a Martensitic Stainless Steel. *Metals* **2020**, *10*, 1620. [[CrossRef](#)]
28. Franceschini, A.; Ruby-Meyer, F.; Midroit, F.; Diawara, B.; Hans, S.; Poulain, T.; Trempont, C.; Hénault, E.; Rouffié, A.-L. An assessment of cleanliness techniques for low alloyed steel grades. *Metall. Res. Technol.* **2019**, *116*, 509. [[CrossRef](#)]
29. Hoyle, G. *Electroslag Processes, Principles and Practice*; Applied Science Publisher Ltd.: New York, NY, USA, 1983; p. 29.
30. Fredriksson, H.; Åkerlind, U. *Materials Processing During Casting*; John Wiley & Sons, Ltd.: Hoboken, NJ, USA, 2006; pp. 27, 185, 207, 219, 265.
31. Mitchell, A. Solidification in remelting processes. *Mater. Sci. Eng. A* **2005**, *413–414*, 10–18. [[CrossRef](#)]
32. Mitchell, A. Industrial effects associated with the columnar to equiaxed transition in remelted ingots. *Int. J. Cast Met. Res.* **2009**, *22*, 216. [[CrossRef](#)]
33. Mitchell, A. *Estimation of Melting Rates, Confidential Internal Report Ordered*; Uddeholms AB: Hagfors, Sweden, 1999.
34. Fredriksson, H.; Jarleborg, O. Solidification of electroslag remelted ingots. *JOM* **1971**, *23*, 32. [[CrossRef](#)]
35. Korp, J.C. Einfluss der Schmelzrate auf die Charakteristiken nichtmetallischer Einschlüsse beim Elektroschlacke-umschmelzen unter Schutzgas. *BHM* **2012**, *157*, 174–180.
36. Iborodin, I.P.; Gorayainov, V.A.; VKoshman, V.S.; Zaitseva, L.A.; Tsapaeva, L.L. Influence of solidification conditions on dendritic structure and segregation of elements in electroslag remelted ingots. *Steel USSR* **1985**, *15*, 533–537.
37. Xuan, C.; Persson, E.S.; Sevastopolev, R.; Nzotta, M. Motion and Detachment Behaviors of Liquid Inclusion at Molten Steel-Slag Interfaces. *Metall. Mater. Trans. B* **2019**, *4*, 1957–1973. [[CrossRef](#)]

-
38. Voronov, V.A. Kinetics of dissolution of MgO in CaF₂ slags. *Izv. Akad. Nauk SSSR Met.* **1975**, *3*, 62–65.
 39. Imagumbai, M. Relationship between Primary- and Secondary-dendrite Arm Spacing of C-Mn Steel Uni-directionally Solidified in Steady State. *ISIJ Int.* **1994**, *34*, 986–991. [[CrossRef](#)]
 40. Kurz, W.; Fischer, D.J. *Fundamentals of Solidification*, 4th ed.; CRC Press: Boca Raton, FL, USA, 1998.